Fully Compensated Synthetic Antiferromagnets with Pronounced Anomalous Hall and Magneto-Optical Responses

Teng Xu,[1,2] Heng-An Zhou,[1,2] Yiqing Dong,[1,2] Qihan Zhang,[1,2] Mengqian Che,[1,2] Liangyang Liu,[1,2] Zhijie Wu,[1,2] Ziqiang Guan,[1,2] Luyi Yang,[1,2] and Wanjun Jiang[1,2,*]

[1] *State Key Laboratory of Low-Dimensional Quantum Physics and Department of Physics, Tsinghua University, Beijing 100084, China*

[2] *Frontier Science Center for Quantum Information, Tsinghua University, Beijing 100084, China*

(Received 31 May 2021; revised 17 August 2021; accepted 13 October 2021; published 28 October 2021)

We report the realization of fully compensated synthetic antiferromagnets (SAFs) in $Pt/Co/Ru/Fe_{1-x}Tb_x$ multilayers with perpendicular magnetic anisotropy, pronounced anomalous Hall resistances and magneto-optical responses. In particular, the properties of SAFs are systematically investigated through optimizing the thicknesses of the Co layer, the Ru spacer, and the concentration (x) of the ferrimagnet (FIM) $Fe_{1-x}Tb_x$ layers. The incorporation of the FIM $Fe_{1-x}Tb_x$ films into SAFs accelerates the search for a magnetic multilayer with fully compensated magnetism and exhibiting pronounced anomalous Hall resistance and magneto-optical signals. These advantages enable spin-orbit-torque switching and magneto-optical Kerr effect imaging experiments on the fully compensated SAFs to be readily investigated. Through incorporating FIMs into SAFs, we believe that the present material system could provide a promising platform not only for adequately addressing the fully compensated spin dynamics of SAFs at room temperature, but also for developing intriguing SAF-based spin-orbitronic devices.

DOI: 10.1103/PhysRevApplied.16.044056

I. INTRODUCTION

Synthetic antiferromagnets (SAFs) made of magnetic multilayers are intriguing alternatives to antiferromagnets for promoting ultradense and ultrafast antiferromagnetic (AFM) like spintronic devices [1]. These magnetic multilayers are typically made of ferromagnet$_1$-nonmagnetic layer (such as Ru or Ir)-ferromagnet$_2$ trilayers ($FM_1/NM/FM_2$), in which the two magnetic layers are coupled through an interlayer Ruderman-Kittel-Kasuya-Yosida (RKKY) interaction, via conduction-electron spin polarization [2–6]. Their applications can be extensively found in giant magnetoresistance and magnetic-tunnel-junction devices [7–12]. Towards spin-orbitronic applications, SAFs with perpendicular magnetic anisotropy (PMA) are of particular importance [13]. For example, a large domain-wall (DW) velocity (up to 750 m/s) [14], chiral-exchange drag [15], synthetic antiferromagnetic skyrmions [16,17], and interlayer chiral Dzyaloshinskii-Moriya interactions [18–20] have been discovered in these SAFs with PMA.

To study the spin dynamics of FM-based SAFs by electrical and optical methods, one needs to slightly adjust the magnetization of the neighboring magnetic layers away from full compensation [21–25]. This is necessary to produce a finite, but small, net uncompensated magnetization ($\vec{M}_{\rm net}$), as shown in the top panel of Fig. 1(a). However, the antiparallel alignment of the two FMs contributes destructively to electrical and optical stimulations. Thus, FM-based (uncompensated) SAFs typically exhibit weak electrical and optical responses. This has been remarked upon previously: "*Synthetic antiferromagnets never entirely compensate*" [26]. In this sense, the exploration of fully compensated SAFs with a vanishing net magnetization ($\vec{M}_{\rm net} = 0$) and pronounced magneto-optical and electrical responses is a great challenge for understanding and, more importantly, for implementing SAF spintronics with zero magnetism. Notably, a fully compensated magnetization state ($\vec{M}_{\rm net} = 0$) can be alternatively achieved in rare-earth transition-metal (RETM) ferrimagnets, which, however, exhibit a stronger anisotropy field (a few tesla) due to antiferromagnetic coupling between the RE and TM sublattices [27–29]. In SAF trilayers, the interlayer exchange coupling is much weaker, which allows for the efficient manipulation of SAFs by magnetic fields, electrical currents, and current-induced spin torques [1]. More importantly, room-temperature fully compensated SAFs can be conveniently obtained via tuning the layer thickness and composition. These are advantages of fully compensated SAFs.

*jiang_lab@tsinghua.edu.cn

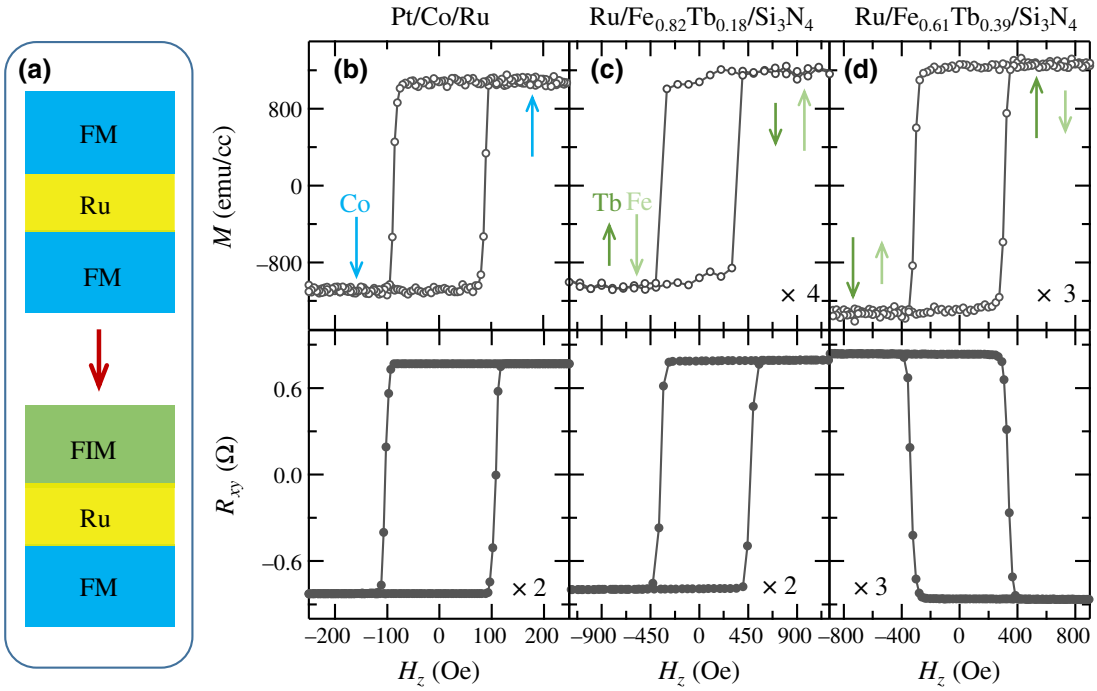

FIG. 1. (a) Schematic illustration of the film stack of SAFs: FM/Ru/FM and FM/Ru/FIM multilayers. Top FM layer will be replaced by a FIM layer in the present study (lower panel). Magnetic hysteresis loops (top panels) and AHE loops (bottom panels) of Pt(3)/Co(1)/Ru(3) multilayer (b), Ru(3)/(Fe-dominated)$Fe_{0.82}Tb_{0.18}(6.5)/Si_3N_4(5)$ multilayer (c), and Ru(3)/(Tb-dominated)$Fe_{0.61}Tb_{0.39}(6.5)/Si_3N_4(5)$ multilayer (d). Blue arrow denotes the magnetization orientation of the Co layer ($\vec{M}_{Co}$). Dark- and light-green arrows represent the antiparallel magnetization orientation of Tb ($\vec{M}_{Tb}$) and Fe ($\vec{M}_{Fe}$) elements, respectively.

Here, we experimentally demonstrate the realization of a class of fully compensated SAFs with PMA at room temperature, together with pronounced electrical and magneto-optical responses in Pt/Co/Ru/$Fe_{1-x}Tb_x$ multilayers. Through replacing one FM layer with a ferrimagnet (FIM) layer of different chemical composition (atomic ratio), $Fe_{1-x}Tb_x$, our material system could be advantageous for studying several key spin-orbitronic properties that are actively discussed for SAFs.

In FIM $Fe_{1-x}Tb_x$ films, the net magnetization is determined by the two oppositely aligned Fe and Tb lattices as follows: $\vec{M}_{Fe\text{-}Tb} = \vec{M}_{Tb} - \vec{M}_{Fe}$. The polar magneto-optical Kerr effect (PMOKE) signal and anomalous Hall effect (AHE) resistance are, however, governed by the magnetization of the 3*d* transition metal Fe, as a result of the relatively low Fermi level of the 4*f* rare earth Tb and its weak coupling with conduction-electron spins [30–33]. Thus, in fully compensated SAFs made of Pt/Co/Ru/$Fe_{1-x}Tb_x$ multilayers, the net magnetization, $\vec{M}_{Fe\text{-}Tb}$, is antiferromagnetically coupled to $\vec{M}_{Co}$, which manifests as a full compensation of magnetization ($\vec{M}_{net} = \vec{M}_{Fe\text{-}Tb} - \vec{M}_{Co} = 0$), as illustrated in the bottom panel of Fig. 1(a). There are, however, pronounced magneto-optical and anomalous Hall responses, simply from the parallel alignment of the transition-metal elements, $\vec{M}_{Co}$ and $\vec{M}_{Fe}$, while in the fully compensated states ($\vec{M}_{net} = 0$). Notably, the magnetic properties of the $Fe_{1-x}Tb_x$ films can be easily tuned through the composition and film thickness, while maintaining a strong PMA [27–29,34,35]. These characteristic features could substantially minimize growth efforts for fabricating fully compensated SAFs with PMA, and enable intriguing spin-orbitronic physics to be conveniently studied from electrical transport, optical, and element-specific approaches.

II. EXPERIMENTS

Magnetic multilayers of stacking order Ta(1)/Pt(3)/Co(t_{Co})/Ru(t_{Ru})/$Fe_{1-x}Tb_x$($t_{Fe\text{-}Tb}$)/Si_3N_4(5) (numbers in parentheses are thicknesses in nanometers) are deposited on thermally oxidized silicon substrates using an AJA magnetron sputtering system (Orion 8). The base pressure of the main chamber is better than 1×10^{-8} torr and the Ar pressure is 3.0 mtorr. A 1-nm-thick Ta layer is used as an adhesive layer and a 5-nm-thick Si_3N_4 layer is used to prevent oxidization of the $Fe_{1-x}Tb_x$ layers. Notably, a Pt(3)/Co(1)/Ru(3) multilayer and a Ru(3)/$Fe_{1-x}Tb_x$(6.5)/Si_3N_4(5) multilayer featuring PMA are also synthesized for comparison. The $Fe_{1-x}Tb_x$ layers are synthesized through cosputtering of the Fe and Tb targets and the chemical composition (x) is adjusted by varying the sputtering power of Tb, while keeping the Fe

sputtering power constant. Magnetic and electrical transport measurements are carried out by using a vibrating sample magnetometer (VSM) and a home-built electrical transport measurement system, respectively. Magnetic multilayers are patterned into Hall bar devices with a channel width of 20 μm by utilizing standard photolithography and Ar-ion milling. Current-induced magnetization switching is performed by injecting a current pulse of 2 ms in duration into Hall bar devices, and the corresponding AHE resistances are subsequently detected using a lock-in amplifier (SR830). The polar Kerr rotation measurements are performed with a home-built MOKE setup using a 633-nm-wavelength He-Ne laser (power $\sim$200 μW), which is focused approximately to a 50-μm spot on the film plane. The polar MOKE microscopy imaging experiments are conducted by using a MOKE imaging microscope from evico magnetics (Dresden). All measurements are performed at room temperature.

III. RESULTS AND ANALYSES

Figure 1(b) presents the perpendicular magnetic hysteresis loop (top panel) and the AHE loop (bottom panel) for a Pt(3)/Co(1)/Ru(3) multilayer, confirming the presence of PMA. The same experiments are also conducted on the Fe-dominated [Ru(3)/$Fe_{0.82}Tb_{0.18}$(6.5)/Si_3N_4(5), $x = 0.18$] and Tb-dominated [Ru(3)/$Fe_{0.61}Tb_{0.39}$(6.5)/Si_3N_4(5), $x = 0.39$] multilayers, which also confirm the existence of PMA, as shown in Figs. 1(c) and 1(d), respectively. Notably, the polarity of the magnetic hysteresis loops ($M - H_z$) are the same for the three samples, since the VSM measures the net magnetization ($\vec{M}_{\rm net} = |\vec{M}_{\rm Fe\,-\,Tb} - \vec{M}_{\rm Co}|$) of the sample. The polarity of the AHE loop ($R_{xy} - H_z$) of Tb-dominated $Fe_{0.61}Tb_{0.39}$ is, however, opposite to the other two, suggesting an antiparallel configuration of $\vec{M}_{\rm Fe}$ with respect to H_z. As mentioned earlier, in $Fe_{1-x}Tb_x$ films, the 3d transition metal Fe dominates the electrical transport property [30–33]. Thus, a sign reversal of AHE loops is expected for Fe-dominated $Fe_{1-x}Tb_x$ ($x = 0.18$) and the Tb-dominated $Fe_{1-x}Tb_x$ ($x = 0.39$) multilayers, as a result of the opposite magnetization orientations of the Fe element. Consequently, the AHE measurement can be used to directly distinguish the magnetism of Tb-dominated $Fe_{1-x}Tb_x$ ($x = 0.39$) from that of Fe-dominated $Fe_{1-x}Tb_x$ ($x = 0.18$) and Co layers, while the net magnetism exhibits a tiny difference. These important characteristics motivate the incorporation of FIM $Fe_{1-x}Tb_x$ films into SAFs in the present study.

Through interfacing two magnetic layers adjacent to a nonmagnetic ultrathin metallic layer, interlayer exchange coupling in the form of an interlayer RKKY interaction, mediates the coupling between the two neighboring magnetic layers (Co and $Fe_{1-x}Tb_x$ layers, in our case). This interlayer coupling oscillates as a function of the interlayer distance ($t_{\rm Ru}$) between the two magnetic layers, which can be tuned from FM to AFM couplings [4–6].

The effect of the Ru spacer in mediating the interlayer RKKY exchange coupling is examined in Pt(3)/Co(1)/Ru($t_{\rm Ru}$)/$Fe_{0.61}Tb_{0.39}$(6.5) multilayers. In this case, the thicknesses of both the Co(1) and $Fe_{0.61}Tb_{0.39}$(6.5) films are fixed, while the thickness of the Ru layer ($t_{\rm Ru}$) is being varied. The $M - H_z$ loops of these multilayers are shown in the top panels of Figs. 2(a)–2(c), in which the squared hysteresis loops confirm the presence of strong PMA. When the Ru spacer is thin ($t_{\rm Ru} < 1$ nm), the bottom Co layer ($\vec{M}_{\rm Co}$) and the top $Fe_{0.61}Tb_{0.39}$ layer ($\vec{M}_{\rm Fe\,-\,Tb}$) are ferromagnetically coupled, resulting in a parallel (ferromagnetic) alignment, which is known as a synthetic ferromagnet (SFM). Through increasing the Ru thickness (1 nm $< t_{\rm Ru} <$ 1.5 nm), interlayer exchange coupling changes from ferromagnetic to antiferromagnetic interactions, resulting in an antiparallel (antiferromagnetic) alignment of the magnetization of Co and $Fe_{0.61}Tb_{0.39}$ layers. This behavior is consistent with the established scenario for SAFs. Notably, interlayer exchange coupling vanishes for a thicker Ru spacer ($t_{\rm Ru} > 1.5$ nm) in which the Co and $Fe_{0.61}Tb_{0.39}$ layers respond differently to magnetic fields and are magnetically decoupled (MDC), as shown in Fig. 2(c). Thus, the onset of antiferromagnetic coupling can be achieved in the Pt(3)/Co(1)/Ru($1 < t_{\rm Ru} < 1.5$)/$Fe_{0.61}Tb_{0.39}$(6.5) multilayers. This is evident from the plateau at zero field, as shown in the top panel of Fig. 2(b).

The corresponding AHE measurements are also carried out and shown in the bottom panels of Figs. 2(a)–2(c). These data further confirm the perpendicular and antiparallel configurations between the Co and $Fe_{0.61}Tb_{0.39}$ layers. It should be mentioned here that the magnetic properties of the 6.5-nm-thick $Fe_{0.61}Tb_{0.39}$ films are dominated by the Tb sublattice, in which the magnetization direction ($\vec{M}_{\rm Tb}$) of the Tb sublattice is parallel to the net magnetization direction ($\vec{M}_{\rm Fe\,-\,Tb} = \vec{M}_{\rm Tb} - \vec{M}_{\rm Fe}$), as well as the external field, while $\vec{M}_{\rm Fe}$ is opposite to the external field, H_z. At zero field, a nearly compensated state ($M_{\rm net} = 36$ emu/cc) in Pt(3)/Co(1)/Ru(1.1)/$Fe_{0.61}Tb_{0.39}$(6.5) is observed. There is, however, a pronounced difference in AHE resistances, which occurs as a result of the same directions of $\vec{M}_{\rm Fe}$ and $\vec{M}_{\rm Co}$ contributing constructively to the AHE resistances, as shown in Fig. 2(b).

The shape of the hysteresis and AHE loops can be understood as follows: magnetization of the Co layer ($\vec{M}_{\rm Co}$) first reverses its direction at -300 Oe (before zero field) and then the net magnetization of the $Fe_{0.61}Tb_{0.39}$ layer ($\vec{M}_{\rm Fe\,-\,Tb}$) reverses its orientation at $+600$ Oe, through sweeping H_z from -1000 to $+1000$ Oe. In the full loop, four different magnetization configurations can be identified, which are schematically illustrated in the bottom panel of Fig. 2(b). Notably, a systematic investigation of the other Pt(3)/Co(1)/Ru($t_{\rm Ru}$)/$Fe_{0.61}Tb_{0.39}$(6.5) SAFs with varied thicknesses of the Ru spacer ($t_{\rm Ru}$) can be

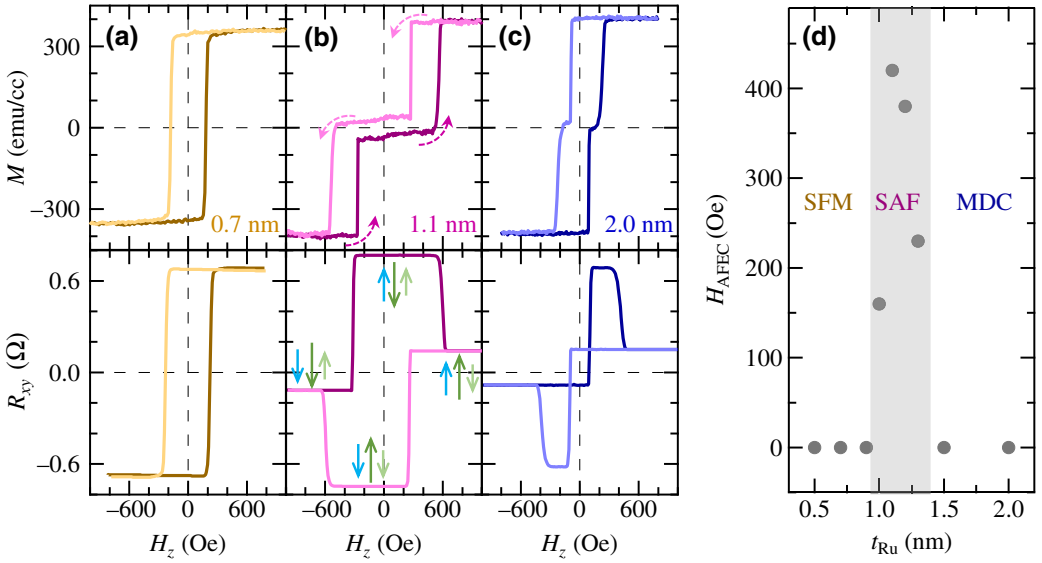

FIG. 2. Magnetic hysteresis loops (top panels) and anomalous Hall effect loops (bottom panels) of $Pt(3)/Co(1)/Ru(t_{Ru})/Fe_{0.61}Tb_{0.39}(6.5)/Si_3N_4(5)$ samples with three different Ru spacer thicknesses (t_{Ru}) of 0.7 nm (a), 1.1 nm (b), and 2.0 nm (c). Dark and light colors represent ascending and descending branches, respectively, of the whole sweeping loop, which is indicated by the dotted line arrows in the top panel of (b). Four different magnetization states are also schematically marked in the bottom panel of (b). Blue arrows denote the magnetizations, $\vec{M}_{Co}$, of the Co layer. Dark- and light-green arrows represent antiparallel magnetizations, $\vec{M}_{Tb}$ and $\vec{M}_{Fe}$, of the FIM $Fe_{1-x}Tb_x$ layers, respectively. (d) Antiferromagnetic exchange-coupling field, H_{AFEC}, as a function of t_{Ru}.

found in Fig. S1 within the Supplemental Material [36], in which similar field-driven multistate switching behaviors are identified.

The AFM exchange-coupling fields, H_{AFEC}, of these $Pt(3)/Co(1)/Ru(t_{Ru})/Fe_{0.61}Tb_{0.39}(6.5)$ SAFs can be quantified by performing minor-loop measurements [37–39], through fixing the layer with a larger coercive field (see Fig. S2 within the Supplemental Material [36]). Figure 2(d) summarizes the evolution of the antiferromagnetic exchange field, H_{AFEC}, as a function of the thickness of the Ru spacer (t_{Ru}). The maximum antiferromagnetic exchange field, H_{AFEC}, can reach 440 Oe in the $t_{Ru} =$ 1.1 nm multilayer.

Through tuning the thickness of the nonmagnetic Ru spacer (t_{Ru}), although we realize SAFs at room temperature, there is, however, finite magnetization ($\vec{M}_{net} = 36$ emu/cc). To demonstrate the realization of fully compensated magnetism ($\vec{M}_{net} = 0$) in the $Pt/Co/Ru/Fe_{1-x}Tb_x$ multilayers, we continue to explore the influence of the chemical composition (x) of the $Fe_{1-x}Tb_x$ layer, while fixing the Ru thickness at $t_{Ru} =$ 1.1 nm. Notably, the chemical composition could directly tune the net magnetization of the $Fe_{1-x}Tb_x$ layers, which, in turn, modulates the interlayer RKKY coupling strengths and types.

The top panels of Fig. 3(a) show the hysteresis loops ($M - H_z$) of $Pt(3)/Co(1)/Ru(1.1)/Fe_{1-x}Tb_x(6.5)$ SAFs with a varying Tb concentration (x). At $x = 0.35$ ($Fe_{0.65}Tb_{0.35}$), it is clear that fully compensated magnetization ($\vec{M}_{net} = \vec{M}_{Fe\text{-}Tb} - \vec{M}_{Co} = 0$) can be obtained at zero magnetic field. In this case, $\vec{M}_{Fe\text{-}Tb}$ and $\vec{M}_{Co}$ are the same amplitude but opposite in orientation. The full cancellation of each other at zero field thus gives rise to fully compensated magnetism. Through changing the Tb concentration (x), the amplitude of $\vec{M}_{Fe\text{-}Tb}$ could be larger or smaller than that of $\vec{M}_{Co}$, resulting in partly compensated SAF states. Figure 3(b) plots the evolution of $\vec{M}_{net}$ (zero field) as a function of Tb concentration (x). Following a decrease in x, the net magnetization, $\vec{M}_{net}$ (at zero field), crosses zero, at which the SAF is fully compensated.

The corresponding AHE loops are also measured and shown in the bottom panels of Fig. 3(a). Following the continuous change of Tb concentration (x), a relatively large change of the AHE resistance, $\Delta R_H = 1.5\ \Omega$, can be observed between the two antiferromagnetic states ($H_z =$ 0). In the Pt/Co/Ru and $Ru/Fe_{0.61}Tb_{0.39}/Si_3N_4$ trilayers, the magnitude of AHE resistances (ΔR_H) are about 0.8 and 0.6 Ω, respectively. This thus demonstrates that the additive AHE responses are achieved in our SAF trilayer. Moreover, the antiferromagnetic exchange field, H_{AFEC} ($H_{AFEC} = 810$ Oe), obtained from the minor loops of Co layers (see Fig. S2 within the Supplemental Material [36]) increases with a decrease in Tb concentration ($x =$ 0.26), which is shown in Fig. 3(c). It is also demonstrated that the antiferromagnetic exchange-coupling field, H_{AFEC}, is modulated through changing the Tb concentration (x) in the FIM $Fe_{1-x}Tb_x$ layer.

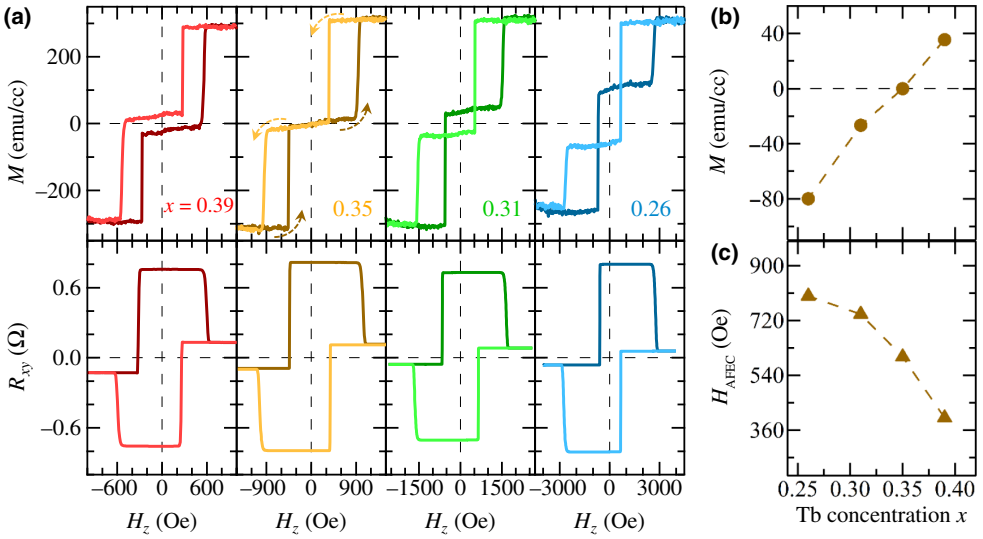

FIG. 3. (a) Hysteresis loops (top panels) and AHE loops (bottom panels) of the Pt(3)/Co(1)/Ru(1.1)/$Fe_{1-x}Tb_x$(6.5)/Si_3N_4(5) SAFs with varying Tb concentration ($x = 0.39$, 0.35, 0.31, and 0.26). (b) Net magnetization, $\vec{M}_{net}$, at zero external field as a function of Tb concentration (x). Dotted line is zero net magnetization of the fully compensated SAF ($\vec{M}_{net} = 0$). (c) Evolution of the antiferromagnetic exchange-coupling fields, H_{AFEC}, as a function of Tb concentration (x) for Pt(3)/Co(1)/Ru(1.1)/$Fe_{1-x}Tb_x$(6.5)/Si_3N_4(5) SAFs.

Similarly, fully compensated magnetism can be achieved by changing the thickness of the Co layer (t_{Co}) in Pt(3)/Co(t_{Co})/Ru(1.1)/$Fe_{0.61}Tb_{0.39}$(6.5), by fixing the thickness of the Ru spacer (1.1 nm) and the thickness of the FIM $Fe_{0.61}Tb_{0.39}$ layer (6.5 nm), as shown in Fig. 4. There, one can find that the increasing thickness, and hence, increasing total magnetic moment of the Co layer, continuously modulates the level of magnetization compensation at zero field. In particular, a fully compensated SAF is evident with $t_{Co} = 1.2$ nm.

In the following, we continue to reveal the accompanied magneto-optical responses by performing PMOKE measurements. Measurements are done in a typical polar Kerr configuration, in which the laser beam is reflected at normal incidence and the external field is applied perpendicular to the sample plane (along the laser incidence direction) [40]. Specifically, three representative samples are studied: Pt(3)/Co(1)/Ru(3), Ru(3)/$Fe_{0.61}Tb_{0.39}$(6.5)/Si_3N_4(5), and Pt(3)/Co(1)/Ru(1.1)/$Fe_{0.61}Tb_{0.39}$(6.5)/Si_3N_4(5). The corresponding Kerr hysteresis loops ($\theta_K - H_z$) are shown in Figs. 5(a)–5(c). For these trilayers, both the shapes and field dependences of the $\theta_K - H_z$ loops are consistent with the AHE results. In Pt/Co/Ru/$Fe_{0.61}Tb_{0.39}$/Si_3N_4, the magnitude of the saturated Kerr rotation, $\theta_K \sim 1.5$ mrad, in the fully compensated state is observed, which is larger than the ferromagnet- ($\theta_K \sim 1.0$ mrad in Pt/Co/Ru) and ferrimagnet-based ($\theta_K \sim 1.1$ mrad in

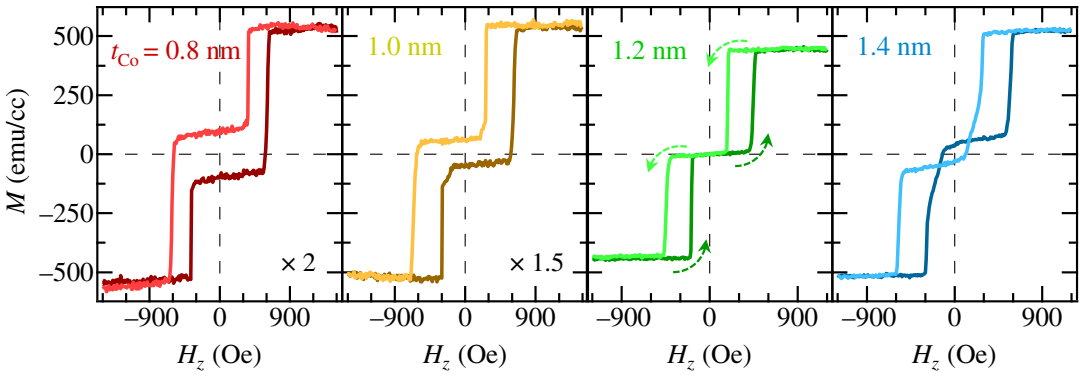

FIG. 4. Perpendicular magnetic hysteresis loops of Pt(3)/Co(t_{Co})/Ru(1.1)/$Fe_{0.61}Tb_{0.39}$(6.5)/Si_3N_4(5) SAFs with varying Co-layer thickness (t_{Co}). Notably, Co layer of 1.4 nm exhibits weak PMA compared with Co layers of 0.8, 1.0, and 1.2 nm. Net magnetization of Pt(3)/Co(1.2)/Ru(1.1)/$Fe_{0.61}Tb_{0.39}$(6.5)/Si_3N_4(5) SAF vanishes and the fully compensated SAF can be achieved through optimizing the thickness of the Co layer.

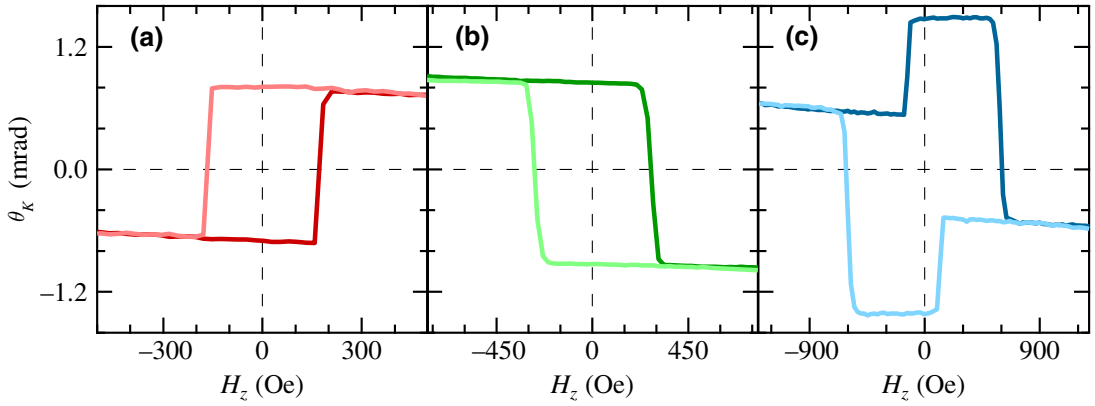

FIG. 5. Hysteresis loops from polar MOKE magnetometry, in which Kerr rotation, θ_K, as a function of perpendicular magnetic field (H_z) is measured in multilayers of (a) Pt(3)/Co(1)/Ru(3), (b) Ru(3)/$Fe_{0.61}Tb_{0.39}$(6.5)/Si_3N_4(5), and (c) Pt(3)/Co(1)/Ru(1.1)/$Fe_{0.61}Tb_{0.39}$(6.5)/Si_3N_4(5).

$Ru/Fe_{0.61}Tb_{0.39}/Si_3N_4$) multilayers. Therefore, even the net magnetization ($\vec{M}_{\text{net}} = \vec{M}_{\text{Fe - Tb}} - \vec{M}_{\text{Co}} = 0$) is fully compensated at zero field ($H_z = 0$); the same orientation of $\vec{M}_{\text{Co,Fe}}$ in the SAFs contributes constructively to the PMOKE signals.

The spin-orbitronic responses of the fully compensated SAFs, through performing current-induced spin-orbit torque (SOT) switching, are subsequently examined [41–44]. Notably, current-induced SOT switching is studied in Co-Fe/Ru/Co-Fe [45], Co/Ir/Co [25], Co-Fe-B/Ta/Co-Fe-B [46,47], (Co/Pt/Co)/Ru/(Co/Pt/Co) [23], and (Co/Pd/Co)/Ru/(Co/Pd/Co) [24,48] with uncompensated magnetization. Arising from the spin Hall effect of the heavy-metal Pt layer, current-induced SOT can be implemented for electrically manipulating the fully compensated magnetism in $Pt/Co/Ru/Fe_{1-x}Tb_x$ multilayers. More importantly, pronounced differences in the AHE resistance ($\Delta R_H \approx 1.5\ \Omega$) of the two opposite and fully compensated antiferromagnetic states enable its reliable readout. This is another distinct difference of our material system, compared with other uncompensated SAFs with extremely weak AHE resistance that are frequently discussed.

The optical image of the Hall bar device made from the fully compensated Pt(3)/Co(1)/Ru(1.1)/$Fe_{0.65}Tb_{0.35}$(6.5) SAF is given in Fig. 6(a). The current-driven SOT-switching measurements are performed with in-plane fields, $H_x = \pm 1000$ Oe, that are required for deterministic switching. Figure 6(b) shows current-driven SOT switching as a function of the current pulse (2 ms) of different amplitudes. It can be seen that the switching polarity reverses after applying opposite in-plane fields, which is consistent with the established SOT-switching scheme. The switching process in the Pt(3)/Co(1)/Ru(1.1)/$Fe_{0.65}Tb_{0.35}$(6.5) SAF can be understood as follows: during SOT switching, magnetization of the Co layer ($\vec{M}_{\text{Co}}$) is directly switched by current-induced SOT from the spin Hall effect of the adjacent Pt layer. Subsequently, $\vec{M}_{\text{Fe - Tb}}$ is switched by antiferromagnetic exchange-coupling torques between the Co layer and the FIM $Fe_{0.65}Tb_{0.35}$ layer [49,50].

The SOT effective field (ΔH_L) and the effective spin Hall angle ($\theta_{\text{SH}}^{\text{eff}}$) are subsequently quantified by performing the first- and second-harmonic Hall voltage measurements under a low-frequency ac current (J_C) [51–53]. More experimental details and theoretical discussions can be found in Part 3 of the Supplemental Material [36]. The dependence of the current-induced effective field on the applied current density, J_C, is summarized in Fig. S3(c) within the Supplemental Material [36]. Considering the longitudinal contribution, the effective spin Hall angle can be derived from the following equation: $\theta_{\text{SH}}^{\text{eff}} = (2e/\hbar)M_s t_{\text{FM}}(\Delta H_L/J_C)$. Here, $\theta_{\text{SH}}^{\text{eff}}$ is the effective spin Hall angle; e is the elementary charge; $\hbar$ is the reduced Planck constant; M_s is the saturated magnetization of the Co layer, assuming that the SOT acts directly only on the Co layer; t_{FM} is the thickness of the magnetic layer. A linear fitting of ΔH_L versus J_C enables $\theta_{\text{SH}}^{\text{eff}} \sim 0.172$ to be obtained, assuming that the SOT acts directly on the adjacent Co layer [23,24].

More importantly, the two fully compensated antiferromagnetically configurations (at zero field), which are switched by the SOTs, can also be electrically readout by the pronounced AHE resistances. Through comparing the resistance changes induced by magnetic fields, one can conclude nearly 100% switching of fully compensated magnetization by the current-induced SOTs. A switching phase diagram summarizing the critical switching current density (J_C) and external in-plane fields (H_x) is given in Fig. 6(c). Following the increase of H_x, J_C decreases monotonously, which occurs as a result of the reduced energy barrier between the two antiferromagnetic states.

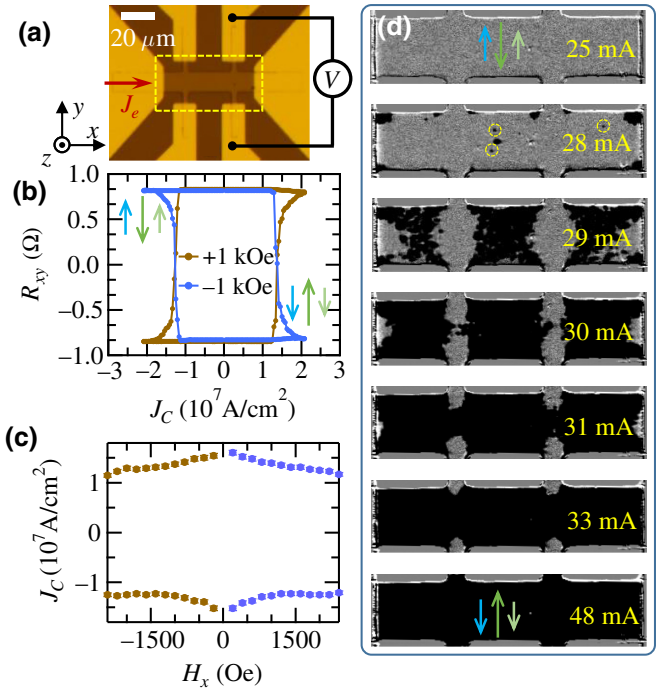

FIG. 6. (a) Optical image of the Hall bar device made from the fully compensated SAF of stacking order Pt(3)/Co(1)/Ru(1.1)/$Fe_{0.65}Tb_{0.35}$(6.5)/Si_3N_4(5). (b) Current-induced SOT-switching measurements performed with in-plane fields of ±1 kOe. Two switched states are two fully compensated antiferromagnetic configurations, as schematically shown in Fig. 2(b). (c) Switching phase diagram acquired at different in-plane fields, H_x. (d) Polar MOKE images at subsequent current pulses during SOT switching with in-plane field of −1 kOe (along the current direction). Isolated SAF magnetic bubbles are indicated by yellow dotted circles in (d).

Notably, current-induced SOT-switching data acquired under different in-plane fields can be found in Fig. S4 within the Supplemental Material [36].

By utilizing polar MOKE microscopy, we not only demonstrate the pronounced magneto-optical contrast of these fully compensated SAFs, but also directly verify current-induced SOT switching in the fully compensated SAFs. Similar to the spin-dependent transport and PMOKE signals, the contrast changes during the PMOKE imaging experiment are also dominated by the magnetizations, $\vec{M}_{Co,Fe}$, in these SAFs. Figure 6(d) displays the PMOKE images that are obtained under different amplitudes of current pulses, in the presence of an in-plane field of −1 kOe along the current direction. Following the increased amplitudes of the current pulse, one can evidently identify that SOT switching takes place through DW nucleation and expansion [54–57]. In particular, a few isolated bubblelike domains are identified during the switching process. Considering the presence of the chiral intralayer (Pt/Co interface) and (possible) chiral interlayer coupling in the present material system [18–20], one may expect the chiral nature of these isolated magnetic bubbles in both the Co and FeTb layers, which will be investigated in the future.

IV. CONCLUSION

Through replacing a ferromagnetic layer by a ferrimagnetic layer of composition $Fe_{1-x}Tb_x$, we experimentally demonstrate the realization of fully compensated SAFs in Pt/Co/Ru/$Fe_{1-x}Tb_x$ multilayers. Since the FIM $Fe_{1-x}Tb_x$ exhibits a bulk perpendicular magnetic anisotropy, the present material system could largely minimize growth efforts in making SAFs with PMA. Furthermore, the choice of the FIM $Fe_{1-x}Tb_x$ film produces pronounced AHE and PMOKE responses in the fully compensated SAFs with zero net magnetization. Through optimizing the thickness of the Co layer, the Ru layer, and the concentration (x) of the FIM $Fe_{1-x}Tb_x$ layers, the magnetic and transport properties of the fully compensated Pt/Co/Ru/$Fe_{1-x}Tb_x$ multilayers are systematically investigated. Current-driven SOT switching, together with pronounced AHE resistances and PMOKE responses of the fully compensated SAFs are also demonstrated. Our material system could be useful for studying several intriguing SAF-based chiral spin-orbitronic phenomena. For example, through optimizing the interlayer and intralayer chiral-exchange interaction in these multilayers, one can easily explore the formation and dynamics of the fully compensated SAF domain walls and skyrmions, by electrical, optical, and element-specific means. Thus, the present material system may hold promise for SAF-related spin-orbitronic devices.

ACKNOWLEDGMENTS

Work carried out at Tsinghua is supported by the Basic Science Center Project of NSFC (Grant No. 51788104), the National Key R&D Program of China (Grant No. 2017YFA0206200), the National Key R&D Program of China (Grants No. 2016YFA0302300 and No. 2020YFA0308800), the National Natural Science Foundation of China (Grants No. 11774194, No. 51831005, No. 1181101082, No. 11804182, and No. 12074212), Beijing Natural Science Foundation (Grant No. Z190009), Tsinghua University Initiative Scientific Research Program, and the Beijing Advanced Innovation Center for Future Chip (ICFC).

[1] R. A. Duine, K.-J. Lee, S. S. P. Parkin, and M. D. Stiles, Synthetic antiferromagnetic spintronics, Nat. Phys. **14**, 217 (2018).

[2] P. Grünberg, R. Schreiber, Y. Pang, M. B. Brodsky, and H. Sowers, Layered Magnetic Structures: Evidence for Antiferromagnetic Coupling of Fe Layers Across Cr Interlayers, Phys. Rev. Lett. **57**, 2442 (1986).

[3] M. N. Baibich, J. M. Broto, A. Fert, F. N. Van Dau, F. Petroff, P. Etienne, G. Creuzet, A. Friederich, and J. Chazelas, Giant Magnetoresistance of (001)Fe/(001)Cr Magnetic Superlattices, Phys. Rev. Lett. **61**, 2472 (1988).

[4] S. S. P. Parkin, N. More, and K. P. Roche, Oscillations in Exchange Coupling and Magnetoresistance in Metallic Superlattice Structures: Co/Ru, Co/Cr, and Fe/Cr, Phys. Rev. Lett. **64**, 2304 (1990).

[5] S. S. P. Parkin, Systematic Variation of the Strength and Oscillation Period of Indirect Magnetic Exchange Coupling Through the 3d, 4d, and 5d Transition Metals, Phys. Rev. Lett. **67**, 3598 (1991).

[6] J. Unguris, R. J. Celotta, and D. T. Pierce, Observation of Two Different Oscillation Periods in the Exchange Coupling of Fe/Cr/Fe(100), Phys. Rev. Lett. **67**, 140 (1991).

[7] J. Hayakawa, S. Ikeda, Y. M. Lee, R. Sasaki, T. Meguro, F. Matsukura, H. Takahashi, and H. Ohno, Current-Induced magnetization switching in MgO barrier based magnetic tunnel junctions with CoFeB/Ru/CoFeB synthetic ferrimagnetic free Layer, Japan, J. Appl. Phys. **45**, L1057 (2006).

[8] S. Parkin, J. Xin, C. Kaiser, A. Panchula, K. Roche, and M. Samant, Magnetically engineered spintronic sensors and memory, Proc. IEEE **91**, 661 (2003).

[9] N. Smith, S. Maat, M. J. Carey, and J. R. Childress, Coresonant Enhancement of Spin-Torque Critical Currents in Spin Valves with a Synthetic-Ferrimagnet Free Layer, Phys. Rev. Lett. **101**, 247205 (2008).

[10] S.-W. Lee and K.-J. Lee, Current-induced magnetization switching of synthetic antiferromagnetic free layer in magnetic tunnel junctions, J. Appl. Phys. **109**, 07C904 (2011).

[11] A. Bergman, B. Skubic, J. Hellsvik, L. Nordström, A. Delin, and O. Eriksson, Ultrafast switching in a synthetic antiferromagnetic magnetic random-access memory device, Phys. Rev. B **83**, 224429 (2011).

[12] D. Houssameddine, J. F. Sierra, D. Gusakova, B. Delaet, U. Ebels, L. D. Buda-Prejbeanu, M. C. Cyrille, B. Dieny, B. Ocker, J. Langer, and W. Maas, Spin torque driven excitations in a synthetic antiferromagnet, Appl. Phys. Lett. **96**, 072511 (2010).

[13] B. Dieny and M. Chshiev, Perpendicular magnetic anisotropy at transition metal/oxide interfaces and applications, Rev. Mod. Phys. **89**, 025008 (2017).

[14] S.-H. Yang, K.-S. Ryu, and S. Parkin, Domain-wall velocities of up to 750ms−1 driven by exchange-coupling torque in synthetic antiferromagnets, Nat. Nanotechnol. **10**, 221 (2015).

[15] S.-H. Yang, C. Garg, and S. S. P. Parkin, Chiral exchange drag and chirality oscillations in synthetic antiferromagnets, Nat. Phys. **15**, 543 (2019).

[16] T. Dohi, S. DuttaGupta, S. Fukami, and H. Ohno, Formation and current-induced motion of synthetic antiferromagnetic skyrmion bubbles, Nat. Commun. **10**, 5153 (2019).

[17] W. Legrand, D. Maccariello, F. Ajejas, S. Collin, A. Vecchiola, K. Bouzehouane, N. Reyren, V. Cros, and A. Fert, Room-temperature stabilization of antiferromagnetic skyrmions in synthetic antiferromagnets, Nat. Mater. **19**, 34 (2020).

[18] D.-S. Han, K. Lee, J.-P. Hanke, Y. Mokrousov, K.-W. Kim, W. Yoo, Y. L. W. van Hees, T.-W. Kim, R. Lavrijsen, C.-Y. You, H. J. M. Swagten, M.-H. Jung, and M. Kläui, Long-range chiral exchange interaction in synthetic antiferromagnets, Nat. Mater. **18**, 703 (2019).

[19] A. Fernández-Pacheco, E. Vedmedenko, F. Ummelen, R. Mansell, D. Petit, and R. P. Cowburn, Symmetry-breaking interlayer dzyaloshinskii–moriya interactions in synthetic antiferromagnets, Nat. Mater. **18**, 679 (2019).

[20] E. Y. Vedmedenko, P. Riego, J. A. Arregi, and A. Berger, Interlayer Dzyaloshinskii-Moriya Interactions, Phys. Rev. Lett. **122**, 257202 (2019).

[21] R. Lavrijsen, A. Fernández-Pacheco, D. Petit, R. Mansell, J. H. Lee, and R. P. Cowburn, Tuning the interlayer exchange coupling between single perpendicularly magnetized CoFeB layers, Appl. Phys. Lett. **100**, 052411 (2012).

[22] M. S. Gabor, T. Petrisor, R. B. Mos, M. Nasui, C. Tiusan, and T. Petrisor, Interlayer exchange coupling in perpendicularly magnetized Pt/Co/Ir/Co/Pt structures, J. Phys. D: Appl. Phys. **50**, 465004 (2017).

[23] C. Bi, H. Almasi, K. Price, T. Newhouse-Illige, M. Xu, S. R. Allen, X. Fan, and W. Wang, Anomalous spin-orbit torque switching in synthetic antiferromagnets, Phys. Rev. B **95**, 104434 (2017).

[24] P. X. Zhang, L. Y. Liao, G. Y. Shi, R. Q. Zhang, H. Q. Wu, Y. Y. Wang, F. Pan, and C. Song, Spin-orbit torque in a completely compensated synthetic antiferromagnet, Phys. Rev. B **97**, 214403 (2018).

[25] Q. Ma, Y. Li, Y.-s. Choi, W.-C. Chen, S. J. Han, and C. L. Chien, Spin orbit torque switching of synthetic Co/Ir/Co trilayers with perpendicular anisotropy and tunable interlayer coupling, Appl. Phys. Lett. **117**, 172403 (2020).

[26] V. Baltz, A. Manchon, M. Tsoi, T. Moriyama, T. Ono, and Y. Tserkovnyak, Antiferromagnetic spintronics, Rev. Mod. Phys. **90**, 015005 (2018).

[27] P. Hansen, C. Clausen, G. Much, M. Rosenkranz, and K. Witter, Magnetic and magneto-optical properties of rare-earth transition-metal alloys containing Gd, Tb, Fe, Co, J. Appl. Phys. **66**, 756 (1989).

[28] V. G. Harris, K. D. Aylesworth, B. N. Das, W. T. Elam, and N. C. Koon, Structural Origins of Magnetic Anisotropy in Sputtered Amorphous Tb-Fe Films, Phys. Rev. Lett. **69**, 1939 (1992).

[29] B. Hebler, A. Hassdenteufel, P. Reinhardt, H. Karl, and M. Albrecht, Ferrimagnetic Tb–Fe alloy thin films: Composition and thickness dependence of magnetic properties and all-optical switching, Front. Mater. **3**, 8 (2016).

[30] J. Finley and L. Liu, Spin-Orbit-Torque Efficiency in Compensated Ferrimagnetic Cobalt-Terbium Alloys, Phys. Rev. Appl. **6**, 054001 (2016).

[31] R. Mishra, J. Yu, X. Qiu, M. Motapothula, T. Venkatesan, and H. Yang, Anomalous Current-Induced Spin Torques in Ferrimagnets Near Compensation, Phys. Rev. Lett. **118**, 167201 (2017).

[32] H. Wu, Y. Xu, P. Deng, Q. Pan, S. A. Razavi, K. Wong, L. Huang, B. Dai, Q. Shao, G. Yu, X. Han, J.-C. Rojas-Sánchez, S. Mangin, and K. L. Wang, Spin-orbit torque switching of a nearly compensated ferrimagnet by topological surface states, Adv. Mater. **31**, 1901681 (2019).

[33] K. Cai, Z. Zhu, J. M. Lee, R. Mishra, L. Ren, S. D. Pollard, P. He, G. Liang, K. L. Teo, and H. Yang, Ultrafast and energy-efficient spin–orbit torque switching in compensated ferrimagnets, Nat. Electron. **3**, 37 (2020).

[34] Y. Mimura and N. Imamura, Magnetic properties of amorphous Tb-Fe thin films prepared by rf sputtering, Appl. Phys. Lett. **28**, 746 (1976).

[35] E. Haltz, R. Weil, J. Sampaio, A. Pointillon, O. Rousseau, K. March, N. Brun, Z. Li, E. Briand, C. Bachelet, Y. Dumont, and A. Mougin, Deviations from bulk behavior in TbFe(Co) thin films: Interfaces contribution in the biased composition, Phys. Rev. Mater. **2**, 104410 (2018).

[36] See the Supplemental Material at http://link.aps.org/supplemental/10.1103/PhysRevApplied.16.044056 for additional information on Ru-spacer dependence, AFM exchange-coupling fields, second-harmonic Hall voltage measurements, and in-plane field dependence of SOT switching.

[37] R. B. Morgunov, E. I. Kunitsyna, A. D. Talantsev, O. V. Koplak, T. Fache, Y. Lu, and S. Mangin, Influence of the magnetic field sweeping rate on magnetic transitions in synthetic ferrimagnets with perpendicular anisotropy, Appl. Phys. Lett. **114**, 222402 (2019).

[38] Y. Ishikuro, M. Kawaguchi, T. Taniguchi, and M. Hayashi, Highly efficient spin-orbit torque in Pt/Co/Ir multilayers with antiferromagnetic interlayer exchange coupling, Phys. Rev. B **101**, 014404 (2020).

[39] K. Wang, L. Qian, S.-C. Ying, and G. Xiao, Manipulation of the interlayer exchange coupling in perpendicular magnetized thin films via tunable magnetic-layer and spacer thicknesses, Phys. Rev. B **102**, 144430 (2020).

[40] A. Hubert and R. Schäfer, *Magnetic Domains: The Analysis of Magnetic Microstructures* (Springer-Verlag Berlin Heidelberg, Berlin, 1998).

[41] I. M. Miron, K. Garello, G. Gaudin, P.-J. Zermatten, M. V. Costache, S. Auffret, S. Bandiera, B. Rodmacq, A. Schuhl, and P. Gambardella, Perpendicular switching of a single ferromagnetic layer induced by in-plane current injection, Nature **476**, 189 (2011).

[42] L. Liu, O. J. Lee, T. J. Gudmundsen, D. C. Ralph, and R. A. Buhrman, Current-Induced Switching of Perpendicularly Magnetized Magnetic Layers Using Spin Torque From the Spin Hall Effect, Phys. Rev. Lett. **109**, 096602 (2012).

[43] L. Liu, C.-F. Pai, Y. Li, H. W. Tseng, D. C. Ralph, and R. A. Buhrman, Spin-Torque switching with the giant spin Hall effect of tantalum, Science **336**, 555 (2012).

[44] A. Manchon, J. Železný, I. M. Miron, T. Jungwirth, J. Sinova, A. Thiaville, K. Garello, and P. Gambardella, Current-induced spin-orbit torques in ferromagnetic and antiferromagnetic systems, Rev. Mod. Phys. **91**, 035004 (2019).

[45] Y.-C. Lau, D. Betto, K. Rode, J. M. D. Coey, and P. Stamenov, Spin–orbit torque switching without an external field using interlayer exchange coupling, Nat. Nanotechnol. **11**, 758 (2016).

[46] G. Y. Shi, C. H. Wan, Y. S. Chang, F. Li, X. J. Zhou, P. X. Zhang, J. W. Cai, X. F. Han, F. Pan, and C. Song, Spin-orbit torque in MgO/CoFeB/Ta/CoFeB/MgO symmetric structure with interlayer antiferromagnetic coupling, Phys. Rev. B **95**, 104435 (2017).

[47] W. J. Kong, C. H. Wan, B. S. Tao, C. Fang, L. Huang, C. Y. Guo, M. Irfan, and X. F. Han, Study of spin-orbit torque induced magnetization switching in synthetic antiferromagnet with ultrathin Ta spacer layer, Appl. Phys. Lett. **113**, 162402 (2018).

[48] R. Chen, Q. Cui, L. Liao, Y. Zhu, R. Zhang, H. Bai, Y. Zhou, G. Xing, F. Pan, H. Yang, and C. Song, Reducing dzyaloshinskii-moriya interaction and field-free spin-orbit torque switching in synthetic antiferromagnets, Nat. Commun. **12**, 3113 (2021).

[49] S.-H. Yang and S. Parkin, Novel domain wall dynamics in synthetic antiferromagnets, J. Phys.: Condens. Matter **29**, 303001 (2017).

[50] R. Bläsing, T. Ma, S.-H. Yang, C. Garg, F. K. Dejene, A. T. N'Diaye, G. Chen, K. Liu, and S. S. P. Parkin, Exchange coupling torque in ferrimagnetic Co/Gd bilayer maximized near angular momentum compensation temperature, Nat. Commun. **9**, 4984 (2018).

[51] J. Kim, J. Sinha, M. Hayashi, M. Yamanouchi, S. Fukami, T. Suzuki, S. Mitani, and H. Ohno, Layer thickness dependence of the current-induced effective field vector in Ta|CoFeB|MgO, Nat. Mater. **12**, 240 (2013).

[52] K. Garello, I. M. Miron, C. O. Avci, F. Freimuth, Y. Mokrousov, S. Blügel, S. Auffret, O. Boulle, G. Gaudin, and P. Gambardella, Symmetry and magnitude of spin–orbit torques in ferromagnetic heterostructures, Nat. Nanotechnol. **8**, 587 (2013).

[53] M. Hayashi, J. Kim, M. Yamanouchi, and H. Ohno, Quantitative characterization of the spin-orbit torque using harmonic Hall voltage measurements, Phys. Rev. B **89**, 144425 (2014).

[54] A. Thiaville, S. Rohart, É Jué, V. Cros, and A. Fert, Dynamics of dzyaloshinskii domain walls in ultrathin magnetic films, EPL (Europhysics Letters) **100**, 57002 (2012).

[55] O. J. Lee, L. Q. Liu, C. F. Pai, Y. Li, H. W. Tseng, P. G. Gowtham, J. P. Park, D. C. Ralph, and R. A. Buhrman, Central role of domain wall depinning for perpendicular magnetization switching driven by spin torque from the spin Hall effect, Phys. Rev. B **89**, 024418 (2014).

[56] S. Emori, E. Martinez, K.-J. Lee, H.-W. Lee, U. Bauer, S.-M. Ahn, P. Agrawal, D. C. Bono, and G. S. D. Beach, Spin Hall torque magnetometry of Dzyaloshinskii domain walls, Phys. Rev. B **90**, 184427 (2014).

[57] D. Bhowmik, M. E. Nowakowski, L. You, O. Lee, D. Keating, M. Wong, J. Bokor, and S. Salahuddin, Deterministic domain wall motion orthogonal To current flow Due To spin orbit torque, Sci. Rep. **5**, 11823 (2015).